

Article

# Image Interpretability of nSight-1 Nanosatellite Imagery for Remote Sensing Applications

Paidamwoyo Mhangara <sup>1,2,\*</sup>, Willard Mapurisa <sup>1</sup> and Naledzani Mudau <sup>1</sup>

<sup>1</sup> South African National Space Agency, Innovation Hub, Pretoria 0087, South Africa; wmapurisa@sansa.org.za (W.M.); nmudau@sansa.org.za (N.M.)

<sup>2</sup> School of Geography, Archeology and Environmental Studies, University of Witwatersrand, 1 Jan Smuts Avenue, Braamfontein 2000, Johannesburg, South Africa

\* Correspondence: paidamwoyom@yahoo.com

Received: 24 December 2019; Accepted: 18 February 2020; Published: 25 February 2020



**Abstract:** Nanosatellites are increasingly being used in space-related applications to demonstrate and test scientific capability and engineering ingenuity of space-borne instruments and for educational purposes due to their favourable low manufacturing costs, cheaper launch costs, and short development time. The use of CubeSat to demonstrate earth imaging capability has also grown in the last two decades. In 2017, a South African company known as Space Commercial Services launched a low-orbit nanosatellite named nSight-1. The demonstration nanosatellite has three payloads that include a modular designed SCS Gecko imaging payload, FIPEX atmospheric science instrument developed by the University of Dresden and a Radiation mitigation VHDL coding experiment supplied by Nelson Mandela University. The Gecko imager has a swath width of 64 km and captures 30 m spatial resolution images using the red, green, and blue (RGB) spectral bands. The objective of this study was to assess the interpretability of nSight-1 in the spatial dimension using Landsat 8 as a reference and to recommend potential earth observation applications for the mission. A blind image spatial quality evaluator known as Blind/Referenceless Image Spatial Quality Evaluator (BRISQUE) was used to compute the image quality for nSight-1 and Landsat 8 imagery in the spatial domain and the National Imagery Interpretability Rating Scale (NIIRS) method to quantify the interpretability of the images. A visual interpretation was used to propose some potential applications for the nSight1 images. The results indicate that Landsat 8 OLI images had significantly higher image quality scores and NIIRS results compared to nSight-1. Landsat 8 has a mean of 19.299 for the image quality score while nSight-1 achieved a mean of 25.873. Landsat 8 had NIIRS mean of 2.345 while nSight-1 had a mean of 1.622. The superior image quality and image interpretability of Landsat could be attributed for the mature optical design on the Landsat 8 satellite that is aimed for operational purposes. Landsat 8 has a GDS of 30-m compared to 32-m on nSight-1. The image degradation resulting from the lossy compression implemented on nSight-1 from 12-bit to 8-bit also has a negative impact on image visual quality and interpretability. Whereas it is evident that Landsat 8 has the better visual quality and NIIRS scores, the results also showed that nSight-1 are still very good if one considers that the categorical ratings consider that images to be of good to excellent quality and a NIIRS mean of 1.6 indicates that the images are interpretable. Our interpretation of the imagery shows that the data has considerable potential for use in geo-visualization and cartographic land use and land cover mapping applications. The image analysis also showed the capability of the nSight-1 sensor to capture features related to structural geology, geomorphology and topography quite prominently.

**Keywords:** nanosatellites; remote sensing; image quality; image interpretability; land use and land cover applications

## 1. Introduction

The use of miniaturized satellite platforms such as microsatellite and nanosatellites for earth imaging has been gaining momentum globally over the last decade [1–6]. Trends in miniaturization of low earth orbit earth observation satellites witnessed over the last few decades have been driven by universities, commercial satellite operators and space agencies that aim to reduce development cost, reduce launch overheads and scale down development time associated with large satellites such as Landsat, ENVISAT, and Sentinel missions. Traditional large earth observation satellites such as ENVISAT weighed as much as 7.9 megatonnes and NASA's TERRA mission weighed 5.2 megatonnes. Mass is a key determinant in the classification of satellites according to size. Konecny [7] outlines that satellites are usually classified as follows: large satellites (> 1000 kg), medium satellites (500–1000 kg), minisatellites (100–500 kg), microsatellites (10–100 kg), nanosatellites (1–10 kg), picosatellite (0.1–1 kg), and finito satellites (< 100 g). Small satellite missions are shifting the paradigm in earth observation because of their low development cost and short development time makes the development of imaging constellation feasible and mitigates the risk of single-point failures. Small satellite constellations enable more frequent revisit times for time-sensitive applications such as disaster management, crop monitoring, and other time series applications that require high temporal resolution [3,6]. The concept of small satellites has also proven to be attractive due to the opportunities it provides for human capital development in the field of space science and technology and the partnerships forged between high-tech manufacturing small and medium enterprises, universities, and space agencies.

Low cost miniaturized satellite architectures are increasingly proving to be ideal for technology demonstration and scientific experimentation. A trend analysis on civilian earth observation satellites reveals that earth observation spaceborne systems are increasingly moving towards the usage of cheaper miniaturized platforms that use commercial-off-the-shelf (COTS) components [8]. The study further alludes to the growing need for ownership of spaceborne systems by governments and satellite operators to enable greater control of technology and data flows, innovation, and education. The growth in small satellite development is driven by advancements in electronic and computer systems engineering, particularly miniaturization and quantum leaps in performance capability. The emergence of small launch providers on the market has increased low-cost launch opportunities [8–10]. The growth in small satellites has also been supported by the development of smaller and low-cost ground stations with rapid data dissemination mechanisms. Planet Labs have successfully demonstrated the feasibility of using smaller and cheaper satellites for operational and commercial earth observation applications.

The synoptic view provided by satellite images at varying spatial, spectral, and temporal resolutions has optimized the usage of satellite-based earth observations for a range of socio-economic applications such as crop monitoring, human settlements mapping, urban growth assessment, surface water monitoring, vegetation mapping, and post-disaster assessment. In recent years, CubeSats have become the main platform for demonstrating and testing imaging payloads and have been utilized for measuring various land, atmospheric, and ocean parameters. At least 300 CubeSats have been launched since 2000 and it is anticipated that the number of nano and microsatellites will grow exponentially by 2020. While capability demonstration and education has been the main objective of CubeSat programs, the scientific quality of the data produced by CubeSat constellations are frequently exceeding initial expectations. Sarda [11] note that CanX-2 effectively acquired total column measurements of carbon dioxide and GNSS radio occultation measurements.

Since the turn of this decade, the development of nanosatellites commonly known as CubeSats has been gaining traction in South Africa [12]. Cape Peninsula University of Technology's (CPUT) French South African Institute of Technology (F'SATI) pioneered the development and launch of South Africa's first CubeSat known as ZACUBE-1 (codenamed TshepisoSAT) that was launched on 21 November 2013. While ZACUBE-1 was primarily aimed at ionospheric studies and carries an HF beacon as its primary instrument, it has onboard a low-resolution wide swath imager as a secondary payload. As a follow-on mission, CPUT developed a second CubeSat known as ZACUBE-2 that carries onboard a medium resolution matrix imager and a number of communication subsystems aimed at providing AIS

(Automated Information Service) and VDES (VHF Data Exchange Service) data to support maritime domain awareness services [12,13]. In 2017, another South African company developed a nanosatellite known as nSight-1 that was launched as part of the European Commission-funded international QB50 constellation [14]. The nanosatellite was developed over 6 months by the Space Commercial Services (SCS) Aerospace Group in partnership with South African space industry partners [15]. nSight-1 weighs 2.5 kg and has a volume of  $10 \times 10 \times 20 \text{ cm}^3$  [14,15]. It has three onboard payloads that include a modular designed SCS Gecko imaging payload, FIPEX atmospheric science instrument supplied by University of Dresden and a Radiation mitigation VHDL coding experiment supplied by Nelson Mandela University [16]. Gecko imaging payload consists of a 30-meter resolution colour red, green, and blue (RGB) 'snapshot' camera with an integrated data storage and image processing system. The imaging payload uses a matrix sensor in snapshot mode that captures RGB images at 5 frames per second. nSight-1 nanosatellite orbits the earth at an altitude of 400 km with a 50-degree inclination. The imaging payload produces RGB images with Bayer patterns that are downlinked through low bandwidth telemetry radio subsystem.

Whereas CubeSats have demonstrated their capability to capture satellite data at a variety of spatial, spectral, radiometric, and temporal resolutions, little is known about their image quality and usability for key land use and land cover mapping applications. Image quality is a major parameter driving the utilization of satellite data. Many studies emphasize the significance of spatial data quality indicators. The growing interest in data quality is partly due to the proliferation of digital services that utilize remote sensing data [17,18]. The Quality Assurance for Earth Observation (QA4EO) initiative points out that all data and derived products must have a Quality Indicator based on a statistically derived value that must be unequivocal and universal in terms of its definition and derivation [18]. Quality indicators could be objectively derived from measurement and calculations or subjectively from expert judgement. Many global missions such as NASA and USGS's Landsat series missions, ESA's Sentinel mission, and NASA's MODIS Aqua and Terra satellite missions are well radiometrically calibrated and their image quality parameters are well documented. In sharp contrast, the image quality parameters for many small satellites are unknown or at least are not in the public domain. In many instances, satellite imagery from most CubeSats is not radiometrically calibrated, limiting the usage of such data in mainstream remote sensing applications.

A variety of image quality assessment methods have been developed to assess satellite image quality in terms of spatial and spectral consistency of data. Satellite image quality is a subject of considerable scientific interest because of its multifaceted nature and has been expressed using several technical parameters such as ground sampling distance (GSD), relative edge response (RER), edge extent (EE), line spread function (LSF), modulation transfer function (MTF) or point spread function (PSF), and signal to noise ratio (SNR) are used to quantitatively characterize the images in terms of sharpness, noise, nonlinearities, and artefacts [19,20]. The National Image Interpretation Rating Scale (NIIRS) is another well-established image quality metric that is used for evaluating image interpretability and defines objects that are discernible in an image using a rating scale of 0 to 9 [21]. Markedly, the most influential parameters that affect image quality are GSD, MTF, and SNR [22,23].

It is estimated that GSD contributes considerably (more than 70%) to visual image interpretability using the National Image Interpretation Rating Scale (NIIRS). The fifth version of the General Image Quality Equation (GIQE) shown below predicts the NIIRS is largely based on SNR, RER and GSD [22].

$$\text{NIIRS} = A_0 + A_1 \cdot \text{Log}_{10}(\text{GSD}) + A_2 \cdot \left[ 1 - \exp\left(\frac{A_3}{\text{SNR}}\right) \right] \cdot \text{Log}_{10}(\text{RER}) + A_4 \cdot \text{Log}_{10}(\text{RER})^4 + \frac{A_5}{\text{SNR}} \quad (1)$$

where:

RER = Relative Edge Response

GSD = Ground Sampled Distance

SNR = Signal-to-Noise Ratio

$A_0$  to  $A_5$  = General Image Quality Coefficients 9.57, -3.32, 3.32, -1.9, -2, -1.8 respectively.

Many attempts have been explored to predict NIIRS ratings from the images and their associated metadata [24]. The researchers point out that while the GIQE provides a good estimation of NIIRS, it does not account for atmospheric effects that affect image quality. Leachtenauer [25] evaluated the image quality metric (IQM), just-noticeable-difference (JND) metric, peak signal-to-noise ratio (PSNR), root-mean-square error (RMSE), and maximum absolute difference (MAD) objective quality metrics to assess their predictive perceptual quality difference ratings. The assessment indicated that the IQM developed by Nill et al. (1992) was highly correlated with NIIRS ratings and could be used as an indicator to predict the labor-intensive NIIRS ratings. Similarly, Irvine and Nelson [24] highlight that the IQM based method that predicts NIIRS ratings is reliable and performs well under a variety of conditions. The image quality measure (IQM) developed by Nill [26] provides an objective and automated means of measuring that is highly correlated to NIIRS. The NIIRS ratings are obtained by applying the gradient and intercept values derived from the IQ-NIIRS regression equation [27]. A scale factor translates the power spectrum's inherent scale-independence to scale-dependence to convert the Image Quality to NIIRS ratings. A comparison of visual NIIRS and IQM yielded a correlation coefficient of 0.93.

The spatial frequency power spectrum of digital images holds critical image quality information such as sharpness, contrast, and detailed rendition of the images [26]. Image quality assessments have the potential to provide a quality indicator of data captured by nanosatellites in the absence of metadata containing absolute or relative radiometric calibration information. In general terms, image quality approaches can also be classified to reference-based image quality assessment methods and blind or no-reference based algorithms [28]. While reference-based methods are dependent on pristine imagery as a reference source, blind, or automatic image quality assessment is feasible without the need for reference image through the application of objective blind algorithms that predict quality metrics in the distorted image by computing the deviations from the regularity of natural statistics [29,30]. In most cases, natural images are characterized by particular regular statistical properties that are quantifiably modified by the occurrence of distortions. The luminance parameters of natural images are generally locally normalized and conform to the Gaussian-like distribution. The no-reference image quality assessment is purely spatial and is dependent on a spatial NSS model that does not require co-ordinate domain transformation. The model is highly efficient and is valuable for optimizing image processing techniques such as denoising. Image quality assessment is usually constrained by the absence of reference images. Mittal [29] argues that the quality indicators generated by full reference models are not quality measures in the absolute sense given that these approaches assess fidelity relative to a reference image whose pristine nature is uncertain since all images are inherently prone to distortions. It is therefore argued that the performance of image quality assessment models should ideally be predicated on the correlation with the subjective judgements of quality.

The BRISQUE algorithm is one of the most widely used blind reference methods to assess image quality. BRISQUE was used in the quality assessment of satellite stereo images by Xiong [31] and yielded favorable results compared to the Distortion Identification based Image Verity and INtegrity Assessment Evaluation (DIIVINE), BLind Image Integrity Notator using DCT Statistics-II (BLIINDS-II), Spatial-Spectral Entropy-based Quality (SSEQ), and Blind Image Quality Indices (BIQI). Zhang [32] modified the BRISQUE model to assess ZY3 satellite image degradation caused by atmospheric blurring, clouds, reflectance, sampling, and quantization in urban areas. The method is based on support vector machines and natural scene statistics model derived from the BRISQUE algorithm. The results revealed a correlation between predicted scores and human subjective perception. Jaffe [33] evaluated the image scores generated by the BRISQUE model on GeoEye1, QuickBird2, WorldView2, and WorldView3 satellite images and noted a monotonic decrease with increasing image quality and focal length of the remote sensing system. The BRISQUE model also produced superior results when compared to the no-reference image assessment model based on spatial and spectral entropies developed by Liu [34]. Li [35] used BRISQUE to assess the performance of image dehazing algorithm. In contrast to most blind image quality models, BRISQUE evades the characterization of distortion-specific features such

as ringing, blur, or blocking by measuring the loss of naturalness in the image by computing scene statistics of locally normalized luminance values.

The proliferation of nanosatellites with imaging payloads ushers in new opportunities for remote sensing. The satellite data provided by CubeSats have huge potential to benefit earth observation users involved in cartographic land use and land cover mapping applications and in bridging the data gaps in a time-sensitive application such as disaster management. One of the mission objectives for the nSight-1 CubeSat was to provide the first space flight heritage for the Gecko imager. While this mission objective is sufficient to ascertain the innovative engineering capability of the imager as a demonstrator mission, the mission objectives are silent of the primary earth observation applications the nSight-1 mission seeks to achieve and the expected data quality standards. The selection of the most appropriate image quality parameter to use is largely driven by remote sensing applications. Visual interpretation plays a critical role in cartographic applications and the most meaningful image quality measures are considered to be based on the visual assessments by human observers [26].

Visual analysis of images from nanosatellites is compromised by a range of radiometric and geometric distortions such as random noise, signal-to-noise artefacts, motion blurring, stripping, streaking, banding, blocking, haze, illumination effects, and panoramic defects. Radiometric effects that degrade image interpretability arise from poor sensor performance and atmospheric degradation. Sensor orbital dynamics such as roll, pitch and yaw cause geometric distortions. While these issues are present in large satellites such as Landsat 8 and Sentinel-2 they are exacerbated in small high-velocity low-earth orbit nanosatellites. The interpretability of the images from low-earth orbit CubeSats for application purposes is particularly compromised by motion blur due to the high speeds, wide pointing accuracies, non-fixed orbital path of the imaging system with the earth [36]. Relative motion between the nanosatellite and the scene affects the averaging of image intensities during exposure time causing image blurring. The quality of images from CubeSats is further compromised by data compression techniques used to transmit telemetry to the ground receiving station [37].

The objective of this study is therefore to assess the visual interpretability of images captured by the nSight-1 nanosatellite and to recommend potential earth observation applications for the mission. To achieve this, we used a blind image spatial quality evaluator to compute the visual image interpretability of the imagery and the NIIRS method to quantify the interpretability of the images. Landsat 8 Optical Land Imager (OLI) visible bands as a reference to benchmark the performance of the experimental nSight-1 nanosatellite imagery. Landsat-8 was selected because it is known for its reputable radiometric performance. Its image quality is significantly higher compared to previous Landsat missions due to significantly better signal-to-noise ratios and radiometric uniformity [38,39]. Landsat 8 images show very few image artefacts due to residual banding, striping and nonlinearity [39].

## 2. Datasets and Study Sites

The nSight-1 images used in this study are comprised of the red, blue, and green spectral bands. With a 64 km swath, nSight-1 images are captured at a ground sampling distance of 32 m [14]. The sensor features a Bayer-pattern filter, which captures colour images in the visible region of the electromagnetic spectrum. Real-time onboard computer processing as shown in Figure 1 includes Bayer pattern demosaicing, RGB colour space conversion, and chroma subsampling and thumbnail downsampling [16]. Further colour optimization is applied to the images. The spectral response for the red, blue, and green bands are shown in Figure 2. Wavelengths longer than 720 nm are not taken due to the NIR-blocking filter onboard the nSight-1 imager.

The compression imaging workflow for nSight-1 is shown below.

The following procedures are done using real-time onboard processing: Bayer pattern demosaicing, RGB colour space conversion, chroma subsampling, and thumbnail downsampling while the JPEG compression process is done on the onboard computer [15]. One of the advantages of nSight-1 nanosatellite is that it uses a tasking image acquisition strategy. This entails that the nanosatellite only captures images over targeted areas that have been pre-programmed and does not have a fixed

temporal resolution. Unlike Landsat 8 that mainly operates in systematic acquisition mode, tasking allows frequent revisits over programmed areas of interest.

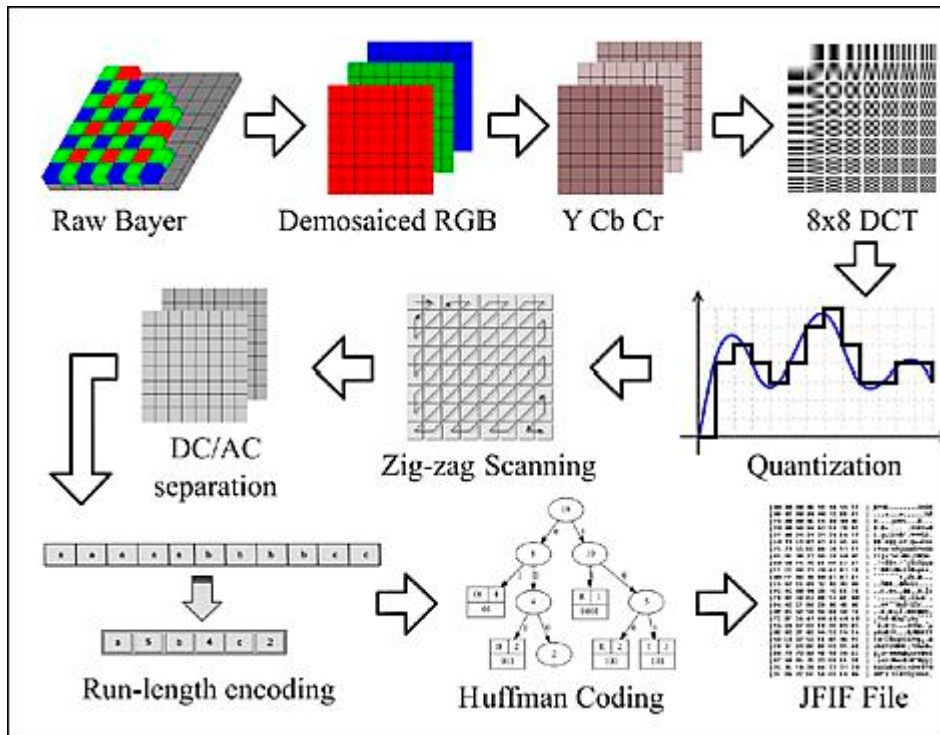


Figure 1. JPEG compression imaging workflow (image credit: SCSAG).

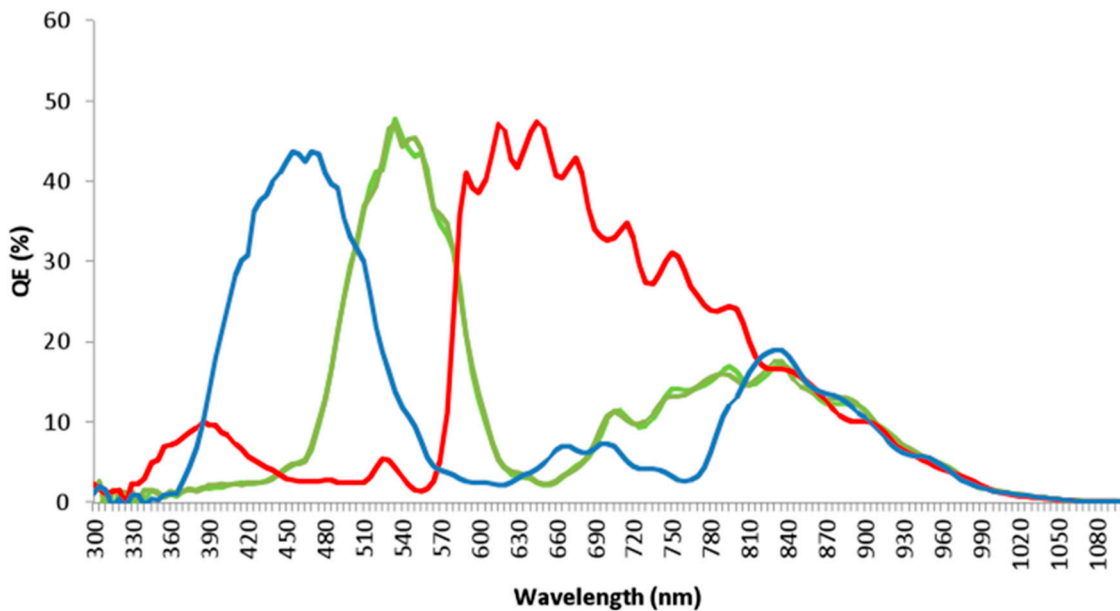


Figure 2. Spectral responses curves for the nSight-1 (image credit: SCSAG).

Landsat 8 images acquired over the study area were used for comparing the image quality score, using the red, blue, and green spectral bands. The Landsat 8 images were selected because nSight-1 and Landsat 8 multispectral bands share the same spatial resolution of 30 m. nSight-1 CubeSat images were acquired from Space Commercial Services and Landsat 8 OLI images from South African National Space Agency. Landsat 8 Operational Land Imager (OLI) and Thermal Infrared Sensor (TIRS) images are received through direct reception at SANSA from NASA and USGS owned Landsat 8 satellite.

Landsat 8 OLI images consist of nine VNIR and SWIR spectral bands at 30 m spatial resolution. The Landsat 8 OLI blue, green, and red spectral bands are strategically designated at 0.452–0.512, 0.533–0.590, and 0.636–0.673 micrometres of the electromagnetic spectrum respectively to capture land cover features such as water, vegetation, soil, and geology. Images used in this study are collected over sites in South Africa, USA, Canada, Botswana, Egypt, Bolivia, and Saudi Arabia. The study sites are characterized by diverse land use and land cover types discernible from nSight-1 nanosatellite images.

### 3. Method

#### 3.1. Estimation of NIIRS Score Using the Image Quality Measure (IQM) Algorithm

In this study, we applied the MITRE Image Quality Measure Computer Program<sup>©</sup> (IQM-v7.3) to automatically compute NIIRS ratings for the images. To establish the NIIRS values for the nSight-1 and reference Landsat 8 images we used the Image Quality Measure (IQM) algorithm. IQM is an objective, quantitative image quality indicator that uses the spatial frequency power spectrum of digital imagery and the modulation transfer function of the human visual system [26]. The power spectrum carries critical spatial quality information inherent in digital images such as sharpness, contrast and detail rendition [40]. IQM is highly correlated with the NIIRS to the extent that IQM valued can easily be converted to NIIRS values using a regression equation. NIIRS is a standard visual quality scale utilized in image interpretation that has been used widely for the detection, recognition and identification of man-made objects discernible from digital satellite imagery and aerial photography. In this study, we used the MITRE Image Quality Measure Computer Program<sup>©</sup> (IQM-v7.3) to compute the NIIRS values for the images. The mathematical formulae for IQM is shown in Equation (2) below.

$$IQM = \frac{1}{M^2} \sum_{\theta} \sum_{\rho} S(\theta_1)W(\rho)A^2(T_{\rho})P(\rho, \theta) \quad (2)$$

where:

- $M^2$  = digital image size in pixels
- $S(\theta_1)$  = directional image scale parameter
- $W(\rho)$  = modified Wiener noise filter
- $A^2(T_{\rho})$  = MTF of the human visual system ( $T$ = constant)
- $P(\rho, \theta)$  = brightness normalized image power spectrum
- $(\rho, \theta)$  = spatial frequency in polar coordinates

The program is capable of computing NIIRS for general aerial images, space digital sensors, space oblique digital sensor, and digitized film imagery.

#### 3.2. Blind/Referenceless Image Spatial Quality Assessment

In this study, we use the Blind/Referenceless Image Spatial Quality Evaluator (BRISQUE) to assess the visual-spatial image quality of nSight-1 imagery. The BRISQUE model uses scene statistics of locally normalized luminance coefficients to characterize possible losses of naturalness in the image as a result of distortions [29]. We selected BRISQUE due to its computational simplicity and superior performance over other complex methods. Mittal [29] reported that BRISQUE produced better results compared traditional methods involving full-reference peak signal-to-noise ratio (PSNR) and structural similarity index (SSIM). BRISQUE uses a Natural Scene Statistics model framework of pair-wise products locally normalized luminance values to compute an automatic measure of perceptual quality in the spatial domain without the use of a reference image [29,30]. The algorithm does not use distortions specific features such as blur to calculate image quality losses. The results of the image considered to be highly correlated. BRISQUE is increasingly being used in a variety of satellite image quality assessments. The image quality scores computed by the BRISQUE Model are expressed in a grading scale of 0 to 100 where a score of 0 is indicative of the best quality and 100 is considered the worst. Translating this

to the equivalent categorical five-level scales (excellent, good, fair, poor, bad) implies 0 is excellent and 100 is poor. This approach is beneficial since other blind image quality assessment methods are distortion specific and are only able to perform that assessment when there is prior knowledge to the distortion affecting the image such as blur, compression, and noise.

### 3.3. Statistical Analysis

To compare the image quality scores and NIIRS values for nSight-1 and Landsat 8 images we performed a statistical analysis in GraphPad Prism8<sup>®</sup> software. The Shapiro–Wilk test was first used to test the normal distribution of the visual scores from the blind assessment image quality scores and NIIRS scores while a Student’s *t*-test was used to compare the score from the two datasets using a significance level of 0.05.

### 3.4. Assessment of Potential Applications Using Visual Image Interpretation

Visual image interpretation was used to discern land use and land cover features distinguishable from the images to recommend potential remote sensing applications for nSight-1 CubeSat images. McGlone [41] defines image interpretation as the process of examining images by identifying objects and judging their significance. Image interpretation is a fundamental step in most image analysis and classification procedures and has been taking place since the advent of aerial photography and persists to present-day remote sensing [41–43]. Elements of image interpretation such as tone, colour, size, shape, texture, pattern, shadow height, depth, volume, slope, aspect and higher-order elements of the site, situation, and associations were used to perform accurate image interpretation. Recently, Kuffer [44] used the primitive elements of image interpretation to describe the physical characteristics of slums. The scholars subsequently used the observed image characteristics as a precursor in developing advanced image classification algorithms. In our current study, we used collateral information such as global land use and land cover maps, Google Earth, geological maps, and street maps as the search method to correlate our image interpretation. Image interpretation keys were also used to aid the analysis.

## 4. Results and Discussion

The results for the blind image spatial quality assessment and the NIIRS evaluation are shown in Tables 1 and 2 for nSight-1 and Landsat 8 respectively. The Shapiro–Wilk test results confirmed a normal distribution for the image quality score and NIIRS variables for both nSight-1 and Landsat 8. The normality test for the NIIRS values using an alpha value of 0.05 was positive as shown by a *p*-value of 0.8651 and 0.7949 for nSight-1 and Landsat 8 respectively. The Shapiro–Wilk test *p*-values for the visual scores were 0.3314 and 0.3469 for the nSight-1 and Landsat 8 respectively. The two-tailed *t*-test results indicate that Landsat 8 OLI images yielded significantly higher visual quality scores and NIIRS results compared to Landsat 8 OLI, indicative of Landsat 8’s superior image quality and better image interpretation compared to nSight-1. The mean for Landsat 8 is 19.299 and nSight-1 it is 25.873 for the image quality score. Landsat 8 had NIIRS mean of 2.345 while nSight-1 had a mean of 1.622. The statistical significance of between the image quality scores is reflected by a *p*-value of 0.0373 and NIIRS for NIIRS assuming a 95% confidence interval.

**Table 1.** nSight-1 image quality and interpretability assessment

| Image Location          | Image Quality Score | Categorical 5 Level Scale | NIIRS    |
|-------------------------|---------------------|---------------------------|----------|
| Bolivia, Salar de Uyuni | 36.3078             | Good                      |          |
| Botswana, Okavango      | 36.831              | Good                      | 1.77501  |
| Canada                  | 14.4916             | Excellent                 | 2.08289  |
| Egypt                   | 37.5298             | Good                      |          |
| Greece                  | 20.5761             | Good                      | 1.8977   |
| Saudi Arabia, Mecca     | 10.4605             | Excellent                 | 0.616793 |

**Table 1.** *Cont.*

| Image Location          | Image Quality Score | Categorical 5 Level Scale | NIIRS   |
|-------------------------|---------------------|---------------------------|---------|
| USA, Bear Lake Utah     | 33.3418             | Good                      |         |
| USA, Delano California  | 23.6812             | Good                      | 1.75470 |
| USA, Houston            | 15.8594             | Excellent                 | 2.64145 |
| South Africa Brandvlei  | 37.5934             | Good                      | 2.40621 |
| South Africa Garapie    | 19.113              | Excellent                 | 1.06132 |
| South Africa Hermanus   | 19.9483             | Excellent                 | 2.47380 |
| South Africa Klipplaat  | 46.5608             | Fair                      | 1.49862 |
| South Africa Loskop     | 18.162              | Excellent                 | 1.65338 |
| South Africa Vredefort  | 17.7154             | Excellent                 | 1.26504 |
| South Africa Wild coast | 7.1196              | Excellent                 |         |

**Table 2.** Landsat 8 image quality and interpretability assessment

| Image Location          | Image Quality Score | Categorical 5 Level Scale | NIIRS   |
|-------------------------|---------------------|---------------------------|---------|
| Bolivia, Salar de Uyuni | 17.4271             | Excellent                 | 1.93204 |
| Botswana, Okavango      | 24.9815             | Good                      | 2.64529 |
| Canada                  |                     |                           |         |
| Egypt                   | 14.2259             | Excellent                 | 1.68207 |
| Greece                  | 25.4605             | Good                      | 3.51831 |
| Saudi Arabia, Mecca     | 16.2534             | Excellent                 | 1.76295 |
| USA, Bear Lake Utah     | 19.013              | Excellent                 | 2.71126 |
| USA, Delano California  | 19.7489             | Excellent                 | 2.75540 |
| USA, Houston            |                     |                           |         |
| South Africa Brandvlei  | 21.8291             | Good                      | 2.80659 |
| South Africa Garapie    | 17.6915             | Excellent                 | 0.98958 |
| South Africa Hermanus   | 2.77804             | Excellent                 | 3.36128 |
| South Africa Klipplaat  | 31.0834             | Good                      | 1.82553 |
| South Africa Loskop     | 17.6015             | Excellent                 | 2.15515 |
| South Africa Vredefort  | 15.5129             | Excellent                 | 1.87964 |
| South Africa Wild Coast | 22.9926             | Excellent                 | 2.63885 |

A summary of the statistical test for the referenceless image spatial assessment and NIIRS evaluation is shown in Tables 3 and 4 respectively and are graphically depicted by the box and whisker plots in Figures 3 and 4.

**Table 3.** Image quality score *t*-test statistical summary

| Image Quality Score    | nSight-1 | Landsat 8 |
|------------------------|----------|-----------|
| Mean                   | 26.06719 | 19.04281  |
| Standard deviation     | 11.81379 | 6.5620978 |
| Standard error of mean | 3.157369 | 1.7537944 |
| N                      | 14       | 14        |
| Confidence interval:   | 95%      |           |
| <i>P</i> -value        | 0.0373   |           |

The superior image quality and image interpretability of Landsat 8 could be attributed for the mature optical design on the Landsat 8 that has been designed for operational purposes. Landsat 8 has

a GDS of 30-m compared to 32-m on nSight-1. GSD is considered to be one of the most influential factors affecting NIIRS. The image degradation that occurs due to the lossy compression implemented on nSight-1 from 12-bit to 8-bit can be considered to lower its image visual quality and interpretability. Whereas it is evident that Landsat 8 has better visual quality and NIIRS scores, the results reveal that when considered independently nSight-1 images are easily interpretable at a NIIRS rating of 1.6 and of good spatial image quality as attested by its mean score of 26 obtained in the referenceless evaluation. Moreover, at the categorical level, the nSight-1 images were largely rated as good to excellent.

**Table 4.** NIIRS *t*-test statistical summary

| NIIRS                  | nSight-1 | Landsat 8  |
|------------------------|----------|------------|
| Mean                   | 1.640257 | 2.369972   |
| Standard deviation     | 0.569861 | 0.78692867 |
| Standard error of mean | 0.180206 | 0.2488487  |
| N                      | 10       | 10         |
| Confidence interval:   | 95%      |            |
| <i>P</i> -value        | 0.0009   |            |

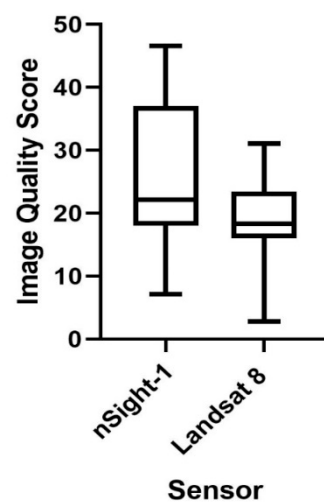


**Figure 3.** Image quality score box and whisker diagram.

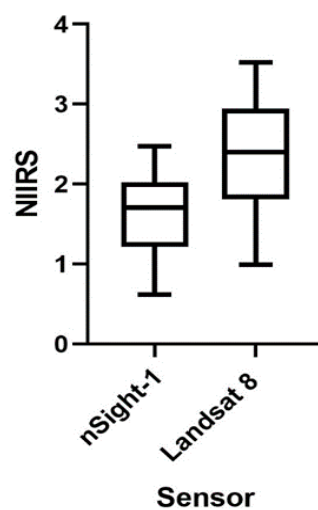


**Figure 4.** NIIRS box and whisker plot.

The visual-spatial quality of nSight-1 imagery could be attributed to the spatial, spectral, and radiometric characteristics of the data. Clarity and identification of objects are substantially influenced by salient image quality parameters such as GSD, MTF, SNR, RER, LSF, and EE. Variations in the NIIRS values obtained in this study could be attributed to factors such as atmospheric haze, contract, angle of obliquity and noise that influence image interpretability. Our visual interpretation results are consistent with NIIRS ratings between 1 and 2.5 computed in this study. At NIIRS 1, we were able to distinguish between key land covers and land use classes such as agriculture, forests, urban and rural areas, geological structures, and drainage morphology; and at NIIRS 2, we identified road networks, large ships, large centre-pivot irrigated fields. It is evident from this study that a medium spatial resolution of 30 m is suitable for discriminating land cover features such as agricultural fields, water bodies, forest patches, settlements, coastline, and roads.

Equally important, the spectral resolution of the imagery in the visible range was fundamental in differentiating the subtle colour variability that reflects the composition within various land cover types. In this case, the location of the imager's spectral bands in the principal (blue, green, and red) wavelengths regions of the visible electromagnetic spectrum proved sufficient for visual analysis. The blue, green and red spectral bands on the nSight-1 imager are valuable for a range of remote sensing applications. While the blue spectral band is prone to substantial atmospheric scattering and absorption, it is useful for mapping land use, water bodies and vegetation characteristics. The green band reacts to the green reflectance of healthy vegetation and accentuates peak vegetation, is therefore quite valuable for assessing plant vigour. nSight-1's red band is located in the red chlorophyll absorption region and is valuable for vegetation discrimination and delineation of geological and soil boundaries.

Radiometric resolution is a major factor that influences the visual quality of satellite imagery. Huete [45] highlights that the radiometric resolution of a sensor is indicative of the fidelity with which the imager can distinguish subtle differences in reflectance and is a function of the sensor signal-to-noise ratio. The optical design of the nSight-1 Gecko imager includes a 2 Mega Pixel RGB sensor unit and the Bayer-pattern filter that positively influences the quality of images captured by the nanosatellite. While the raw images for nSight-1 are captured at 12 bits, the images are downsampled to 8-bit colour images by standard discrete cosine transform lossy 8-bit RGB JPEG compression techniques due to capacity constraints imposed by the onboard computer and satellite power. A radiometric resolution of 8 bits impacts on the visual image quality of nSight-1 nanosatellite data as it controls the actual information contained in the images and shows the sensitivity of the sensor due to small differences in reflected energy. Modern earth observation satellites such as Landsat 8 and Sentinel-2 have radiometric resolutions of 16 bits and older sensors such as Landsat 7 are scaled to 8-bit. Radiometric calibration has not been done to make the data analysis-ready for quantitative time series based remote sensing applications that require accurate Top of the Atmosphere Reflectance or Surface Reflectance values such as trend analysis of vegetation vigour using vegetation indices. Lack of radiometrically calibrated images could be addressed in future nSight missions by installing an onboard radiometric calibration device on the imager. Calibration and validation of the imagery could also be achieved through alternative methods such as vicarious calibration and image cross-calibration. Improving the radiometric data quality will ensure the interoperability of the imagery with different data sources. The potential for radiometric calibration of CubeSat data has been demonstrated by Houborg [46]. Using calibrated CubeSat data from Planetlabs, Houborg [47,48] showed the feasibility of cross-calibration and interoperability of CubeSat data with data from prominent missions such as Landsat 8, Sentinel-2, and MODIS for deriving vegetation parameters such as normalized vegetation index (NDVI) and leaf area index (LAI).

Practical uses for nSight-1 imagery shown in the study include urban demarcation, forestry delineation, mapping of structural geology features, agriculture field boundary extraction, water body mapping, and coastline mapping and assessment, land degradation and soil erosion assessments, drainage morphometric analysis of fluvial systems, wetlands monitoring, maritime ship surveillance, mapping of major roads, general land use, and land cover mapping. A range of nSight-1 applications

has been identified in this study. Visual analysis of nSight-1 images over croplands shows that the images are valuable in supporting food security through the generation crop maps. The images could also be used as a base data source for the extraction of agricultural field boundaries. Images of Delano, USA and Loskop, South Africa reveal rectangular and concentric cropped and fallow agricultural fields. Field boundary information is critical in agricultural field inventories and crop yield estimations. Water is a scarce resource and the frequent monitoring of water body surfaces is important to support effective water resources management. Images of Bear Lake, USA and Brandvlei, South Africa show that nSight-1 image could be applied to monitor dam locations and their surface areal extends, dam inventory and water licencing. Regular monitoring of the surface areal extends of dams is vital in analysing the receding water levels in drought situations and expanded water extends during flood situations. The image for Bolivia Salar de Uyuni vividly shows evidence of soil erosion. Soil erosion degrades farmlands and negatively impacts agricultural productivity. The strong geological expressions depicted in some of the nSight-1 images suggest that the nanosatellite can be used for mapping of structural geology features to support mineral exploration, groundwater studies, and general geological mapping. The image for the Okavango Delta clearly outlines the swampy delta. Swamps perform an important ecological function and their preservation is therefore critical. Data from satellites such as nSight-1 is therefore vital in supporting the frequent monitoring of swamps. Using the image for Mecca in Saudi Arabia we also deduced that nSight-1 can be used to demarcate urbanized areas and subsequently assess urban growth rates. Vegetation cover was identified in most of the images. This entails that nSight-1 has some potential value in the classification of vegetation cover. As shown by the image for the Kithnos island in Greece, nSight-1 images could be used for monitoring ships along coastlines, a function often performed by high spatial resolution optical and radar satellites.

While our visual analysis demonstrates that nSight-1 imagery has a wide range of potential cartographic and land cover applications, the images analyzed exhibited a strong expression of geological structures, geomorphological features, and topography. This finding suggests that the nSight-1 imagery has the potential to contribute substantially to mapping studies linked to structural geology and associated mineralization, geomorphology, and photoclinometry. Given that geological and geomorphological mapping applications are not very time-sensitive, preservations of the captured satellite imagery are required to support future studies. The features discernible from nSight-1 imagery are consistent with level 1 rating described in the National Imagery Interpretability Rating Scale (NIIRS). Table 5 illustrates the nSight-1 images examined in this study and some potential applications for the data.

**Table 5.** Interpretation of nSight-1 images and some potential applications

| nSight-1 Image  | Location                   | Discernible Features                     | Application |
|---|----------------------------|--|-------------|
|  | California,<br>Delano, USA | Cropped and fallow<br>rectangular fields | Agriculture |

Table 5. Cont.

| nSight-1 Image  | Location                          | Discernible Features  | Application   |
|---|-----------------------------------|---|---|
|    | <p>Bear Lake, Utah,<br/>USA</p>   | <p>Dam;<br/>vegetation patches;<br/>bare areas</p>  | <p>Water resources<br/>management;<br/>vegetation<br/>mapping;<br/>analysis of<br/>geological<br/>structures</p>                                      |
|   | <p>Okavango,<br/>Botswana</p>     | <p>Swampy wetland;<br/>river systems</p>  | <p>Wetlands<br/>monitoring;<br/>water resources<br/>monitoring</p>  |
|  | <p>Hermanus,<br/>South Africa</p> | <p>Coastline; water<br/>bodies;<br/>forest patches; ocean;<br/>mountainous<br/>topography with<br/>steep slopes</p> | <p>Coastline<br/>mapping;<br/>maritime<br/>monitoring;<br/>forest mapping;<br/>water resources<br/>management;<br/>structural geology<br/>mapping</p> |

Table 5. Cont.

| nSight-1 Image  | Location                | Discernible Features  | Application   |
|---|-------------------------|---|---|
|    | Kithnos, Greece         | Ships; island; ocean; drainage pattern morphology   | Maritime surveillance and ship detection; structural geology mapping      |
|   | Brandvlei, South Africa | Dam; concentric cropped fields; geological structures; forest patches; open grasslands; drainage morphological patterns | Water resources management, agriculture, forest paths, geological mapping |
|  | Gariiep, South Africa   | Fluvial systems; small water bodies; open grasslands; concentric cropped and fallow agriculture                         | Analysis of fluvial systems; drainage morphometric analysis; agriculture  |

Table 5. Cont.

| nSight-1 Image  | Location                | Discernible Features   | Application  |
|---|-------------------------|--|--|
|    | Klipplaat, South Africa | Geological structures, lineaments, intrusions, bedding trends, lithology, and boundaries; soil erosion features; river system; dryland or degraded landscape | Geological mapping, land degradation, and soil erosion assessments |
|   | Bolivia Salar de Uyuni  | Soil erosion; geological folding; dryland or degraded landscape; drainage pattern morphology   | Land degradation and soil erosion assessment; geological mapping   |
|  | Saudi, Mecca            | Road network; built-up areas   | Urban mapping; mapping of major roads                              |

Table 5. Cont.

| nSight-1 Image   | Location             | Discernible Features  | Application  |
|--|----------------------|---|--|
|   | Loskop, South Africa | Drainage pattern morphology; vegetation patches; river system; cropped and fallow agricultural fields | Drainage analysis; water resources management; land degradation assessment; land cover mapping |
|  | Loskop, South Africa | Concentric cropped and fallow agricultural fields; dam; river system; open grasslands; roads          | Agriculture; water resources management; land cover classification; mapping of major roads     |

The good visual quality of the nSight-1 images in the spatial dimension suggest that the image is potentially valuable in producing accurate land use and land cover maps using on-screen digitizing and other advanced classification approaches such as object-based classification and morphological profiles that exploit spatial information and image characteristics such as shape, size, colour, compactness, and texture.

The variability in the NIIRS could be a result of several factors. While NIIRS values are largely influenced by ground sampling distance and relative edge response, other variables such as the signal to noise ratio, noise gain due to edge sharpening, and geometric mean height of overshoot due to edge sharpening plays a role. The impact of variable factors, such as atmospheric effects on the images due to haze has the potential to affect the results. The results, however, seem to show overall consistency in terms of the NIIRS variability trends between nSight-1 and the reference Landsat 8 data. This may suggest that environmental conditions such as structural landscape features, terrain, build-up features, atmospheric conditions, and illumination conditions affect the assessment of NIIRS values. This was particularly evident in the Okavango Delta, where high values were obtained and the Saudi Arabia Desert where low NIIRS values were derived from both n-Sight-1 and Landsat 8 data. This result was line with our visual observation, that is, in cases where large landscape features are conspicuously defined with a good contrast the NIIRS values were high. This was also true in desert environments

with little contrast, we observed low NIIRS values. This suggests contracting grey-level values driven by tonal variations resulting from background effects might have a bearing on NIIRS.

Considering the small size of the nanosatellite, the analyses of the nSight-1 images undertaken in this study clearly indicates that the RGB images captured by the Gecko Imager are of high quality and are useful for a variety of cartographic and geo-visualization applications. Success could be attributed to the innovative matrix design of the Gecko Imager that uses a Bayer-pattern filter to capture colour images at medium spatial resolution of 30 m, high native radiometric resolution 12 bits that are downsampled to 8-bits and nanosatellite's robust real-time onboard computer processing capabilities. The spatial resolution of the images captured by the Gecko matrix imager could be increased through super-resolution (SR) image reconstruction as demonstrated by Li [28] using the ZY-3 TLC images. Super-resolution image reconstruction will not only transform the low-resolution images into higher-resolution images but will also improve image interpretability. SPOT 5 is a good example of where SR techniques have been used successfully to achieve a 2.5 m resolution image from a 5 m resolution sensor. A detailed overview of single-frame and multi-frame SR methods is provided by many papers [49–51]. Notwithstanding the data downlink challenges imposed by a low bandwidth telemetry radio subsystem, a lossless compression was going to be more advantageous than the lossy compression implemented for nSight in terms of content retention and maintenance of image quality. Furthermore, while acknowledging the capacity constraints imposed by CubeSats in terms of size, weight and data downlinking, an additional near-red spectral band would have widened the applications offered by the satellite. A 64 km swath width available on nSight-1 gives it a competitive advantage over aerial photography due to its ability to cover vast tracks of land in one acquisition. The on-board image processing capability implemented on nSight-1 differentiates this mission from a range of operational satellites and future missions should inherit this novel capability. Whereas our study confirms the value of nSight-1 imagery, follow-up nSight missions will need to consider a wide range of operational remote sensing requirements such as data calibration and data policies. Ground segment operations such as data acquisition, archiving, cataloguing, curatorship, access, and distribution are also critical in ensuring the success of follow-up nSight missions. Potential benefits of developing a constellation of CubeSats whose primary mission objective is dedicated towards remote sensing of land cover parameters should be considered. As shown already by Planet Labs with more than 150 satellite in orbit, a constellation of nSight earth imaging CubeSats could also be used to shorten the revisit times and improve the temporal resolution of the nanosatellites. Such a constellation could leverage technological advancements in cloud computing, big data analytics, and future data architectures such as datacubes to maximize data usage.

## 5. Conclusions

The upsurge in the number of low cost nanosatellites with earth imaging capabilities offers new prospects for earth observation. Although most of the nanosatellites have been used as platforms for education, capability demonstration and testing scientific space-borne instruments, the potential for the usage of CubeSat data for practical remote sensing applications are increasingly being realized. In this study, we assessed the image quality of the satellite images captured by the nSight-1 CubeSat and examined the images to consider the potential remote sensing applications for the mission. Results of this study indicated that Landsat 8 OLI images produced significantly higher image quality scores and NIIRS results compared to nSight-1, revealing Landsat 8 has superior image quality and better image interpretation characteristics. Nonetheless, when considered independently, it can be concluded that nSight-1 images are of high quality as shown by an average NIIRS value of 1.6 and the spatial image quality scores that ranged in the good to excellent image quality categories. The quality of nSight-1 imagery in the spatial dimension is attributable to the inherent spatial, spectral, and radiometric resolution of the data.

Our interpretation of the imagery indicates that the data has considerable potential for use in geo-visualization and cartographic land use and land cover mapping applications. The features

discernible from nSight-1 imagery are consistent with those described at level 1 and 2 of the National Image Interpretability Rating Scales (NIIRS). We observed that inSight-1 imagery could be used for a range of earth observation application that include urban demarcation, forest patch delineation, mapping of structural geology features, agriculture field boundary extraction, water body mapping, and coastline mapping and assessment, land degradation and soil erosion assessments, drainage morphometric analysis of fluvial systems, wetlands monitoring, maritime ship surveillance, mapping of major roads, general land use, and land cover mapping. The nSight-1 images analyzed in the study depicted strong expressions of geological structures, geomorphological patterns, and surface topography. Imagery from the nSight-1 nanosatellite could also be used for filling data gaps in rapid response applications such as disaster management and other time-sensitive applications. To widen its applications, increase data usage, and improve temporal resolution, we recommend in the future that nSight-1 missions investigate developing a constellation of CubeSats with an increased number strategically placed spectral bands in the visible and near-infrared (VNIR) region. The inclusion of the near-infrared band could be prioritized. We also recommend future missions to focus on radiometric calibration to improve the radiometric quality of the data and potentially get the data to an analysis-ready state.

**Author Contributions:** Conceptualization, P.M.; Methodology, P.M.; Validation, P.M., W.M., and N.M.; Formal analysis, P.M., W.M., and N.M.; Investigation, P.M., W.M., and N.M.; Writing—original draft preparation, P.M., W.M., and N.M.; Writing—review and editing, P.M., W.M., and N.M.; Project administration, P.M. All authors have read and agreed to the published version of the manuscript.

**Funding:** This research received no external funding.

**Acknowledgments:** We are highly indebted to Space Commercial Services (SCS) for providing us with nSight-1 imagery used in this study. We particularly extend our appreciation to Francois Malan and Hendrik Burger for providing us with the background technical information regarding nSight-1 necessary for us to proceed with this study.

**Conflicts of Interest:** The authors declare no conflict of interest.

## References

1. Buzzi, P.G.; Selva, D.; Hitomi, N.; Blackwell, W.J. Assessment of constellation designs for earth observation: Application to the TROPICS mission. *Acta Astronaut.* **2019**, *161*, 166–182. [[CrossRef](#)]
2. Esper, J.; Panetta, P.V.; Ryschkewitsch, M.; Wiscombe, W.; Neeck, S. NASA-GSFC nano-satellite technology for earth science missions. *Acta Astronaut.* **2000**, *46*, 287–296. [[CrossRef](#)]
3. Kramer, H.J.; Cracknell, A.P. An overview of small satellites in remote sensing. *Int. J. Remote Sens.* **2008**, *29*, 4285–4337. [[CrossRef](#)]
4. Poghosyan, A.; Golkar, A. CubeSat evolution: Analyzing CubeSat capabilities for conducting science missions. *Prog. Aerosp. Sci.* **2017**, *88*, 59–83. [[CrossRef](#)]
5. Sandau, R.; Brieß, K.; D’Errico, M. Small satellites for global coverage: Potential and limits. *ISPRS J. Photogramm. Remote Sens.* **2010**, *65*, 492–504. [[CrossRef](#)]
6. Selva, D.; Krejci, D. A survey and assessment of the capabilities of Cubesats for Earth observation. *Acta Astronaut.* **2012**, *74*, 50–68. [[CrossRef](#)]
7. Konecny, G.; Str, N.; Hannover, D. *Small Satellites—A Tool for Earth Observation?* University of Hannover: Hannover, Germany, 1957; pp. 4–6.
8. Woellert, K.; Ehrenfreund, P.; Ricco, A.J.; Hertzfeld, H. Cubesats: Cost-effective science and technology platforms for emerging and developing nations. *Adv. Space Res.* **2011**, *47*, 663–684. [[CrossRef](#)]
9. Crisp, N.H.; Smith, K.; Hollingsworth, P. Launch and deployment of distributed small satellite systems. *Acta Astronaut.* **2015**, *114*, 65–78. [[CrossRef](#)]
10. Depasquale, D.; Charania, A.C.; Commercial, S.; Kanayama, H.; Matsuda, S.; Application, F.; From, L.; United, C.; Orbit, L.E.; Picosatellite, O.; et al. Analysis of the earth-to-orbit launch market for nano and microsatellites. In Proceedings of the AIAA SPACE Conference & Exposition, Anaheim, CA, USA, 30 August–2 September 2010; pp. 1–8.

11. Sarda, K.; Eagleson, S.; Caillibot, E.; Grant, C.; Kekez, D.; Pranajaya, F.; Zee, R.E. Canadian advanced nanospace experiment 2: Scientific and technological innovation on a three-kilogram satellite. *Acta Astronaut.* **2006**, *59*, 236–245. [[CrossRef](#)]
12. Steyn, W.H.; Van Zyl, R.; Innggs, M.; Cilliers, P.J. Current and future small satellite projects in South Africa. In Proceedings of the IEEE International Geoscience and Remote Sensing Symposium, Melbourne, Australia, 21–26 July 2013; pp. 1294–1297.
13. Griffith, D.; Cogan, D.; Magidimisha, E.; Van Zyl, R. Flight hardware verification and validation of the K-line fire sensor payload on ZACube-2. In Proceedings of the Fifth Conference on Sensors, MEMS, and Electro-Optic Systems, Skukuza, South Africa, 18–20 September 2019; p. 100.
14. eoPortal Directory. *nSight-1 CubeSat Mission in QB50 Constellation*; eoPortal Directory: Nagano, Japan, 2018.
15. SCS Space. *nSight-1*; SCS Space: Stellenbosch, South Africa, 2017.
16. Malan, D.F.; Wiid, K.; Burger, H.; Visagie, L.; Steyn, W.H. The development of InSight-1—Earth Observation and Science in 2U. In Proceedings of the 31st Annual AIAA/USU Conference on Small Satellite, Logan, UT, USA, 5–10 August 2017; pp. 1–8.
17. Batini, C.; Blaschke, T.; Lang, S.; Albrecht, F.; Abdulmutallab, H.M.; Barsi, Szabó, G.; Kugler, Z. Data quality in remote sensing. *Int. Arch. Photogramm. Remote Sens. Spat. Inf. Sci.* **2017**, *42*, 447–453. [[CrossRef](#)]
18. Yang, X.; Blower, J.D.; Bastin, L.; Lush, V.; Zabala, A.; Masó, J.; Cornford, D.; Díaz, P.; Lumsden, J. An integrated view of data quality in Earth observation. *Philos. Trans. R. Soc. A Math. Phys. Eng. Sci.* **2013**, *371*, 20120072. [[CrossRef](#)] [[PubMed](#)]
19. Bai, J.; Sun, Y.; Chen, L.; Feng, Y.; Liu, J. EO sensor planning for UAV engineering reconnaissance based on NIIRS and GIQE. *Math. Probl. Eng.* **2018**, *2018*. [[CrossRef](#)]
20. Wierzbicki, D.; Fryskowska, A.; Kedzierski, M.; Wojtkowska, M.; Delis, P. Method of radiometric quality assessment of NIR images acquired with a custom sensor mounted on an unmanned aerial vehicle. *J. Appl. Remote Sens.* **2018**, *12*. [[CrossRef](#)]
21. Li, L.; Luo, H.; Zhu, H. Estimation of the image interpretability of ZY-3 sensor corrected panchromatic nadir data. *Remote Sens.* **2014**, *6*, 4409–4429. [[CrossRef](#)]
22. Leachtenauer, J.C.; Malila, W.; Irvine, J.; Colburn, L.; Salvaggio, N. General image-quality equation: GIQE. *Appl. Opt.* **1997**, *36*, 8322–8328. [[CrossRef](#)] [[PubMed](#)]
23. Stoddard, J.; Messinger, D.; Kerekes, J. Effects of CubeSat design parameters on image quality and feature extraction for 3D reconstruction. In Proceedings of the IEEE Geoscience and Remote Sensing Symposium, Quebec City, QC, Canada, 13–18 July 2014; pp. 1995–1998.
24. Irvine, J.M.; Nelson, E. Image quality and performance modeling for automated target detection. In Proceedings of the Automatic Target Recognition XIX, Orlando, FL, USA, 13–14 April 2009; Volume 7335.
25. Leachtdnauer, J.C. Objective quality measures assessment. In Proceedings of the Visual Information Processing XI, Orlando, FL, USA, 30 July 2002; Volume 4736, pp. 9–16.
26. Nill, N.B. Objective image quality measure derived from digital image power spectra. *Opt. Eng.* **1992**, *31*, 813. [[CrossRef](#)]
27. Information, G.; History, B.; Im, O.F.; Overview, P.; Formats, I.; Format, P.G.M.; Format, T.; Format, B.M.P.; Image, C.; Order, B.; et al. *MITRE Image Quality Measure Computer Program*; Text Copyright; The MITRE Corporation: Bedford, MA, USA, 2008; pp. 1–29.
28. Li, S.; Yang, Z.; Li, H. Statistical evaluation of no-reference image quality assessment metrics for remote sensing images. *ISPRS Int. J. Geo-Inf.* **2017**, *6*, 133. [[CrossRef](#)]
29. Mittal, A.; Moorthy, A.K.; Bovik, A.C. No-reference image quality assessment in the spatial domain. *IEEE Trans. Image Process.* **2012**, *21*, 4695–4708. [[CrossRef](#)]
30. Mittal, A.; Moorthy, A.K.; Bovik, A.C. Blind/Referenceless image spatial quality evaluator. In Proceedings of the Conference Record of the Forty Fifth Asilomar Conference on Signals, Systems and Computers, Pacific Grove, CA, USA, 6–9 November 2011; pp. 723–727.
31. Xiong, Y.; Shao, F.; Meng, X.; Zhou, B.; Ho, Y.S. Sparse representation for no-reference quality assessment of satellite stereo images. *IEEE Access* **2019**, *7*, 106295–106306. [[CrossRef](#)]
32. Zhang, Y.; Cui, W.H.; Yang, F.; Wu, Z.C. No-reference image quality assessment for zy3 imagery in urban areas using statistical model. *Int. Arch. Photogramm. Remote Sens. Spat. Inf. Sci.* **2016**, *41*, 949–954. [[CrossRef](#)]
33. Jaffe, L.; Zelinski, M.; Sakla, W. Remote sensor design for visual recognition with convolutional neural networks. *IEEE Trans. Geosci. Remote Sens.* **2019**, *57*, 9090–9108. [[CrossRef](#)]

34. Liu, L.; Liu, B.; Huang, H.; Bovik, A.C. No-reference image quality assessment based on spatial and spectral entropies. *Signal Process. Image Commun.* **2014**, *29*, 856–863. [[CrossRef](#)]
35. Li, J.; Li, G.; Fan, H. Image dehazing using residual-based deep CNN. *IEEE Access* **2018**, *6*, 26831–26842. [[CrossRef](#)]
36. Wu, X.; Wu, F.; Zhao, J. Motion deblurring for space-based imaging on sandroid CubeSats using improved genetic algorithm. *Procedia Comput. Sci.* **2016**, *80*, 2327–2331. [[CrossRef](#)]
37. Techavijit, P.; Chivapreecha, S.; Sukchalerm, P.; Plodpai, A. CubeSat image transmission in JPEG compression: An experiment on high altitude platform. In Proceedings of the 8th International Conference on Knowledge and Smart Technology, Chiangmai, Thailand, 3–6 February 2016; pp. 164–168.
38. Markham, B.; Barsi, J.; Kvaran, G.; Ong, L.; Kaita, E.; Biggar, S.; Czaplá-Myers, J.; Mishra, N.; Helder, D. Landsat-8 operational land imager radiometric calibration and stability. *Remote Sens.* **2014**, *6*, 12275–12308. [[CrossRef](#)]
39. Morfitt, R.; Barsi, J.; Levy, R.; Markham, B.; Micijevic, E.; Ong, L.; Scaramuzza, P.; Vanderwerff, K. Landsat-8 Operational Land Imager (OLI) radiometric performance on-orbit. *Remote Sens.* **2015**, *7*, 2208–2237. [[CrossRef](#)]
40. MITRE. *Image Quality Measure Computer Program; IQM Guide 7.3*; MITRE: McLean, VA, USA, 2008.
41. McGlone, J.C.; Mikhail, E. *Manual of Photogrammetry: American Society for Photogrammetry and Remote Sensing*; Bethesda: Bethel, MD, USA, 2004.
42. Dwivedi, R.S. *Remote Sensing of Soils*; Springer: Berlin/Heidelberg, Germany, 2018; Volume 497.
43. Jensen, J.R. Remote sensing of vegetation. In *Remote Sensing of the Environment: An Earth Resource Perspective*; Pearson: London, UK, 2006; pp. 355–408.
44. Kuffer, M.; Pfeffer, K.; Souza, R.; Baud, I. Extraction of slum areas from VHR imagery using GLCM variance. *IEEE J. Sel. Top. Appl. Earth Obs. Remote Sens.* **2016**, *9*, 1830–1840. [[CrossRef](#)]
45. Huete, A. *Environmental Monitoring and Characterization*; Artiola, J.F., Brusseau, M.L., Pepper, I.L., Eds.; Elsevier Science: Amsterdam, The Netherlands, 2004; pp. 183–206.
46. Houborg, R.; McCabe, M.F. A cubesat enabled spatio-temporal enhancement method (SYSTEM) utilizing planet, landsat and MODIS data. *Remote Sens. Environ.* **2018**, *209*, 211–226. [[CrossRef](#)]
47. Houborg, R.; McCabe, M.F. Daily retrieval of NDVI and LAI at 3 m resolution via the fusion of CubeSat, Landsat, and MODIS data. *Remote Sens.* **2018**, *10*, 890. [[CrossRef](#)]
48. Houborg, R. Combining CubeSat and conventional satellite sensing for daily mapping of in-field LAI. In Proceedings of the AGU Fall Meeting Abstracts, Washington, DC, USA, 10–14 December 2018.
49. Borman, S.; Stevenson, R.L. Super-resolution from image sequences—A review. In Proceedings of the IEEE Midwest Symposium on Circuits and Systems, Notre Dame, IN, USA, 9–12 August 1998.
50. Park, S.C.; Park, M.K.; Kang, M.G. Super-resolution image reconstruction: A technical overview. *IEEE Signal Process. Mag.* **2003**, *20*, 21–36. [[CrossRef](#)]
51. Yue, L.; Zhang, L.; Shen, H.; Li, J.; Yuan, Q.; Zhang, H. Image super-resolution: The techniques, applications, and future. *Signal Process.* **2016**, *128*, 389–408.

